Predicting transition from selective withdrawal to entrainment in two-fluid stratified systems

Sabbir Hassan, C. Dalton McKeon, and Darryl James*
Department of Mechanical Engineering, Texas Tech University, Lubbock, Texas 79409, USA

(Received 4 March 2022; accepted 5 May 2022; published 24 May 2022; corrected 31 May 2022)

Selective withdrawal is a desired phenomenon in transferring oil from large caverns in the U.S. Strategic Petroleum Reserve (SPR), because entrainment of oil at the time during withdrawal poses a risk of contaminating the environment. Motivated to understand selective withdrawal in an SPR-like orientation, we performed experiments in order to investigate the critical submergence depth as a function of critical flow rate. For the experiments, a tube was positioned through a liquid-liquid interface that draws the lower liquid upward, avoiding entrainment of the upper fluid. Analysis of the normal stress balance across the interface produced a Weber number, utilizing dynamic pressure scaling, that predicted the transition to entrainment. Additionally, an inviscid flow analysis was performed assuming an ellipsoidal control volume surface that produced a linear relationship between the Weber number and the scaled critical submergence depth. This analytical model was validated using the experimental data, resulting in a robust model for predicting transition from selective withdrawal to entrainment.

DOI: 10.1103/PhysRevE.105.055109

I. INTRODUCTION

This paper presents experimental data and discusses results using scale analysis and a simplified inviscid analysis that yields a new relationship between two nondimensional terms that predicts the transition from selective withdrawal to viscous entrainment in a two-liquid, immiscible system.

In the U.S. Strategic Petroleum Reserve (SPR), crude oil is stored in underground salt caverns, which have diameters of approximately 60 m and depths of approximately 600 m [1]. In order to add oil to a cavern, brine is pumped out using a pipe that has been lowered through the interface into the brine. At some critical combination of flow rate and depth below the undeformed interface and the inlet to the pipe, oil is also withdrawn during pumping. This marks the transition from selective withdrawal to entrainment. Selective withdrawal, i.e., removal of only the brine, is desirable during this process, because the removed brine is stored as surface water and any oil in it acts as a pollutant. Motivated to understand selective withdrawal in an SPR-like orientation for which we found no published studies, experiments were performed in order to investigate the critical submergence depth as a function of critical flow rate. For the experiments, a tube was positioned through a liquid-liquid interface that draws the lower liquid upward, avoiding entrainment of the upper fluid, i.e., the SPR-like orientation shown in Figs. 1(a)–1(c). The schematic of the complete experimental setup is shown in Fig. 2.

In this paper, we present two approaches to obtain predictive results for the transition from selective withdrawal to entrainment. The first applies dimensional analysis on the interfacial stress balance, while the second uses Bernoulli's principle or Euler's equation for inviscid fluid flow. The paper is organized as follows: Background on selective withdrawal phenomena is provided in Sec. II; a brief description of the experiments conducted is given in Sec. III; the analytical methods and the necessary fit equations are explained in Sec. IV; and finally the paper concludes with discussion of the results and the conclusion in Secs. V and VI, respectively.

II. BACKGROUND

Early research conducted on selective withdrawal of two-layer stratified liquids was an experimental study by Lubin and Springer [2]. The critical height between the floor of a two-liquid tank and the liquid-liquid interface above was predicted as a function of the sink flow rate. Assuming surface tension to be negligible and using Bernoulli's principle, a Froude number (defined as $\mathrm{Fr} = Q_{\mathrm{cr}}/(g'd)^{1/2}$, where, Q_{cr} is the critical flow rate, d is the tube diameter, and g' is the reduced gravity) based on the sink tube diameter was found to be the characteristic nondimensional parameter representing the flow, and a linear relationship between the nondimensional flow rate and the scaled critical depth for their experimental data collapsed their data well.

A more recent experiment was performed by Cohen and Nagel [3] for a liquid-liquid system in which the upper liquid was withdrawn at a fixed rate (similar to secondary orientation but with the withdrawal tube above the interface). For the given system, the authors found the height of the tube above the interface at the moment of entrainment to be proportional to the volumetric flow rate raised to approximately the 0.3 power. The authors were also able to find a scaling relationship that collapsed all hump profiles to a single profile for low Reynolds number flow. A capillary number based on the capillary length was found to be the representative nondimensional number for the flow. Cohen [4] extended the research by including several pairs of fluids resulting in different density

*darryl.james@ttu.edu

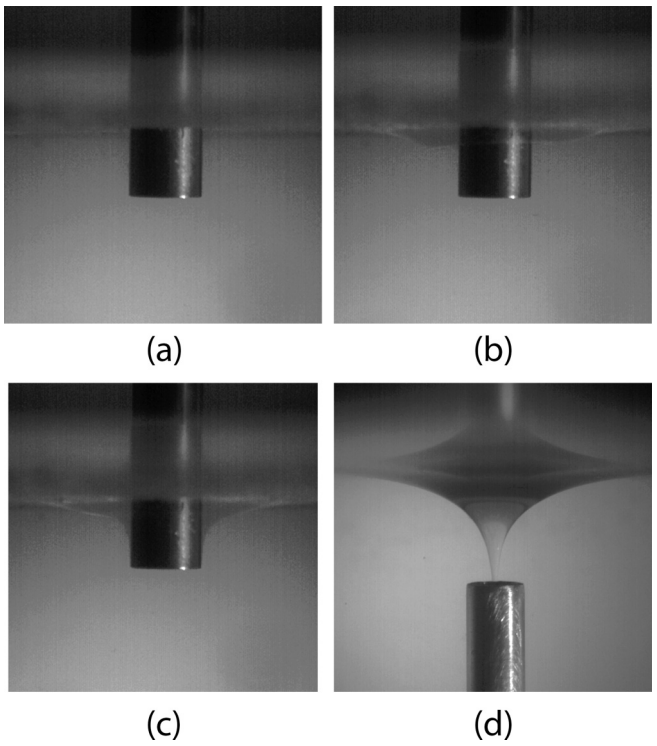

FIG. 1. (a) Primary orientation in an initial state. (b) Primary orientation in a steady, intermediate subcritical flow rate state. (c) Primary orientation just after the inception of entrainment. (d) Secondary orientation just after the inception of entrainment. All the tube inner diameters in the figure are 10.8 mm.

and viscosity ratios. Based on the low Reynolds number assumption, a dimensional analysis led to a relationship between a scaled flow rate and a scaled distance to the undisturbed interface for prediction of the transition to entrainment. The fit equation had the form of a power law with the exponent varying from 0.30 to 0.45, depending on the fluid combinations used in the experiment. Case and Nagel [5] reported a similar relationship in their work while trying to analyze and collapse the spout profiles after entrainment. According to the authors, the spouts have two asymptotic regimes, based on the viscosity ratio, which was matched to each other by the flow dynamics. At large radius, the interface is constrained by gravity to be horizontal and at large heights the spout interface is constrained by the flows in the nozzle to be vertical. The nondimensional flow rate based on the capillary number (defined as $\mathrm{Ca} = \mu_w Q_{\mathrm{cr}}/\gamma l_c^2$, where, Q_{cr} is the critical flow rate, l_c is the capillary length, γ is the interfacial tension, and μ_w is the viscosity of withdrawal fluid) was identified as the representative parameter that collapsed the spout states.

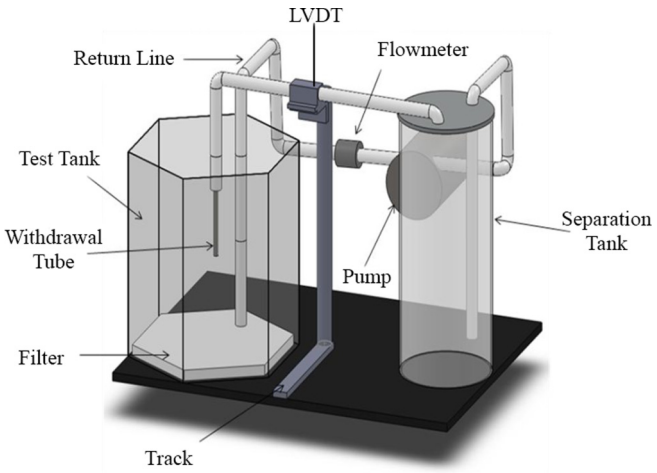

FIG. 2. Schematic diagram of the experimental setup. Cameras (not shown) were located perpendicular to the two faces of the hexagonal test tank [1].

Blanchette and Zhang [6] developed a force balance model to evaluate the system studied experimentally in Cohen paper [4]. According to the authors, the transition to entrainment was dependent on a global force balance on the interface, when the upward force exerted by viscosity because of the withdrawal flow overcomes the downward force of surface tension. The results of the simulation matched the transition trends found in Ref. [4] closely. It was concluded that the interfacial tension was dominated by the weakly deflected portion of the hump far away from the tip. The capillary number (defined as $\mathrm{Ca} = \mu_w Q_{cr}/\gamma S^2$, where Q_{cr} is the critical flow rate, S is the submergence depth, γ is the interfacial tension, and μ_w is the viscosity of withdrawal fluid) was also found to be the representative nondimensional parameter that collapses their data.

In addition to experimental work, the entrainment problem has been investigated numerically. Lister [7] performed a numerical simulation of a two-liquid system of equal viscosity in which a point sink was located a distance above an undeformed interface. Assuming Stokes flow and equal viscosity in both layers, the flow field was solved as a function of capillary number, the sink strength, and a viscous velocity scale. A linear trend in the log-log plot was identified between the nondimensional capillary length and sink strength.

Farrow and Hocking [8] used a two-dimensional finite-difference approach to simulate selective withdrawal of water for high Reynolds number, inviscid, irrotational flow in order to investigate the scatter in the critical draw-down Froude number (defined as $\mathrm{Fr} = Q_{\mathrm{cr}}/(g' S^3)^{1/2}$, where Q_{cr} is the critical flow rate, S is the submergence depth, and g' is the reduced gravity), i.e., transition from selective withdrawal. Their results indicated that interfacial waves could affect the critical draw-down Froude number and were responsible for the experimental scatter observed. The critical draw-down Froude number based on the depth of the withdrawn fluid layer, for conditions in which interfacial waves was not a significant factor, is approximately 1. Later, Hocking *et al.* [9] included the surface tension effect due to the curvature of the interface and concluded that the Froude number, based on the sink depth from the interface, represented the complete flow phenomenon and the surface tension adds a resistance to the withdrawal force. However, no predictive relationship between the submergence depth and the critical flow rate was found.

Initially, the relationships developed in the aforementioned works were applied to our data, but the results were not able to produce a consistent collapse for a predictive relationship between flow rate and submerged depth as shown in Fig. 3. In an attempt to understand the reason for the disparities, we

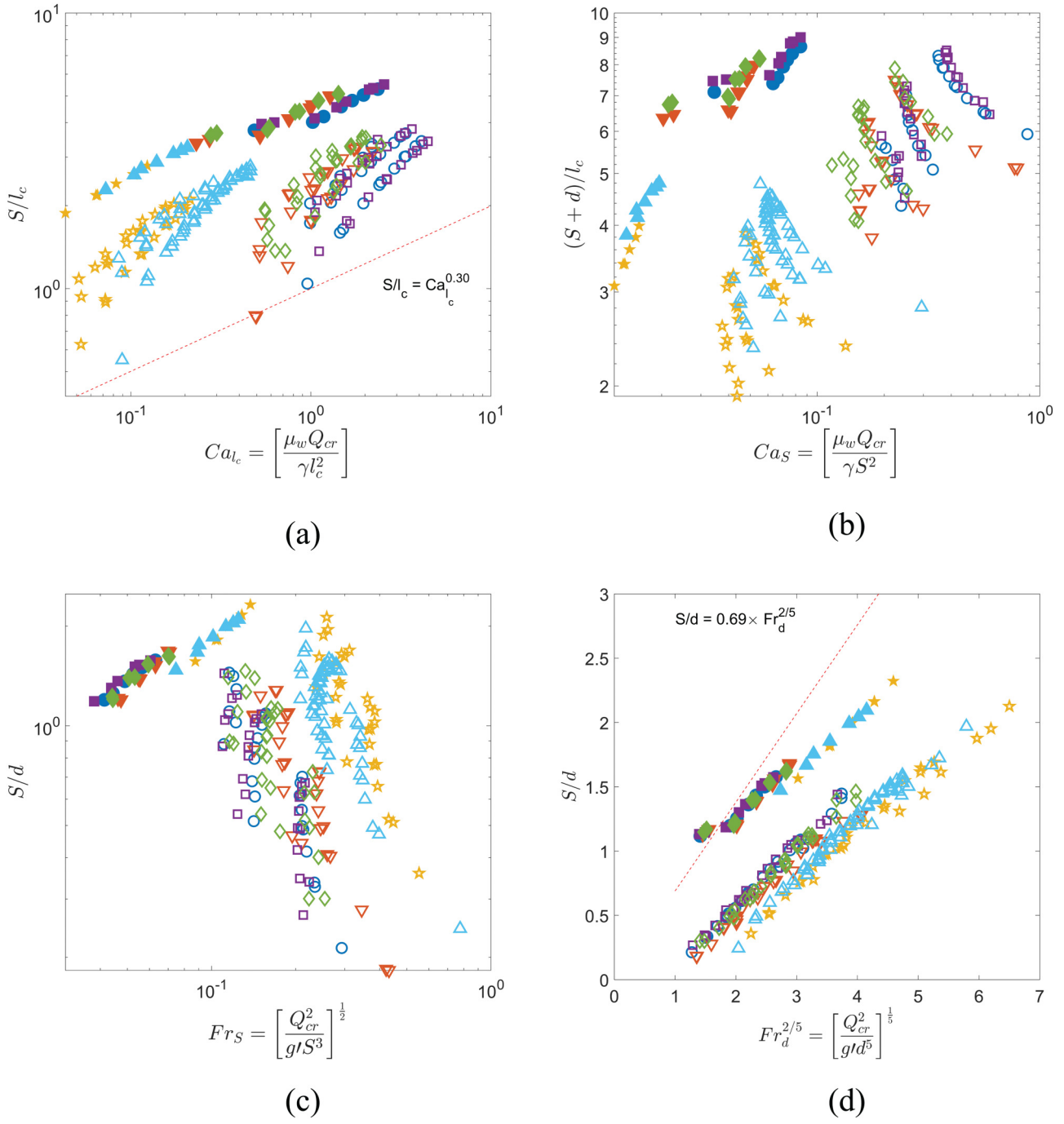

FIG. 3. Plots showing the nondimensional submergence depth as a function of various nondimensional parameters. The secondary orientation data are presented by "filled" symbols, whereas the primary orientation data are presented by "hollow" symbols. The symbols are defined in Table I. (a) Nondimensional submergence depth as a function of capillary number as in Ref. [4]. The dotted red line shows Cohen's correlation. (b) Nondimensional submergence depth as a function of capillary number as in Ref. [6]. (c) Nondimensional submergence depth as a function of Froude number as in Ref. [8]. (d) Nondimensional submergence depth as a function of Froude number as in Ref. [2]. The dotted red line shows Lubin's correlation; see Eq. (15).

consider the flow regime at the onset of entrainment using the Ohnesorge number ($\mathrm{Oh}_{l_c} = \mu_w/(\rho_w \gamma l_c)^{1/2}$, where μ_w is the viscosity of withdrawn fluid, ρ_w is the density of withdrawn fluid, γ is the interfacial tension, and l_c is capillary length), which is defined as the ratio of viscous effect to the combined effect of surface tension and inertia. As fluid is removed at a rate below critical flow rate, the reduction in the pressure due to the withdrawal flow is responsible for the deformation of the interface. In order to maintain the steady deformed interface, the force balance has to be at an equilibrium. For a given subcritical flow rate, at equilibrium, the flow regime effect is not explicitly observable other than causing a change in interface location or shape. But at the onset of entrainment, the interface is swept into the flow and the Ohnesorge number

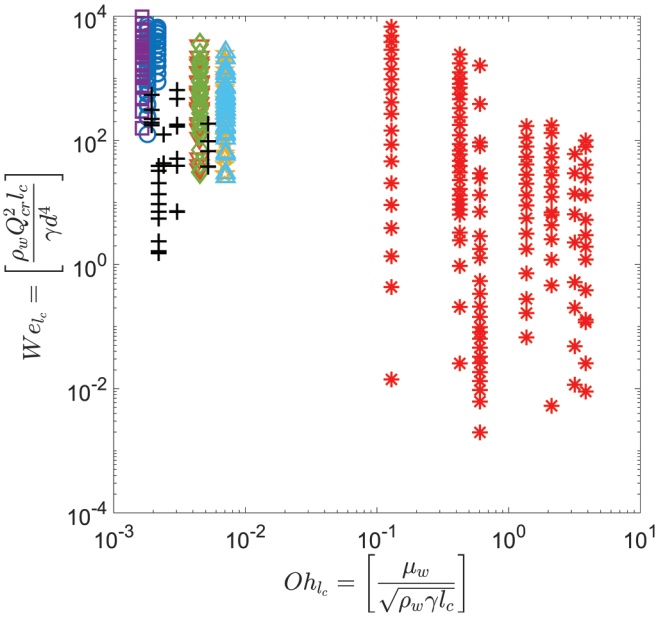

FIG. 4. Weber number as a function of Ohnesorge number. The data from Cohen's experiment are shown using the symbol $*$. The data from Lubin and Springer's experiment are shown using the symbol $+$. The data from this experiment had two orientations. The fluid combinations for the primary and the secondary orientation are expressed using the symbols mentioned in Table I.

and Weber number (defined as $\mathrm{We}_{l_c} = \rho_w U_0^2 l_c/\gamma$, where ρ_w is the density of withdrawal fluid, l_c is capillary length, γ is interfacial tension, and U_0 is the tube velocity) help define the flow regime. Figure 4 shows where the experimental studies fall in comparison to each other in terms of the Weber number and Ohnesorge number. There are three major regimes in terms of the Ohnesorge number. For $\mathrm{Oh}_{l_c} < 0.1$, the viscous effect is negligible compared to the surface tension and inertia effect. For $\mathrm{Oh}_{l_c} > 10$, the viscous effect dominates the surface tension and inertia effect. For $0.1 < \mathrm{Oh}_{l_c} < 10$, the viscous effect is comparable relative to the surface tension and inertia effect. To understand the comparative effect between the surface tension and inertia, the Weber number was also plotted in Fig. 4. For $\mathrm{We}_{l_c} > 1$, the inertia effect dominates over surface tension and for $\mathrm{We}_{l_c} < 1$ the surface tension dominates inertia.

It was found that the Ohnesorge number for our experimental data was very low, meaning during entrainment the viscous effect is negligible compared to the surface tension effect and inertial effect, as shown in Fig. 4. Similarly, Lubin's experimental data are in the regime where viscous effects are also negligible. For both these studies, the Weber numbers are high, meaning surface tension effects were not dominant. Reviewing Cohen's data in Fig. 4, it can be seen that their experimental flow regime overlaps high and low values of We_{l_c} with Oh_{l_c} close to order one; that is, some data are in the region where viscous effect was in a similar order in comparison to the surface tension and inertial effect and also in a region of surface tension dominance. This also explains the possibility of having a hysteresis effect at very low flow rates, as described by Cohen [3,4].

In this paper, we present two approaches that were used to predict transition from selective withdrawal to entrainment for two withdrawal orientations—a dimensional analysis based on the normal stress balance and an extension to a simplified inviscid model. No paper in the literature was found that studied withdrawal of bottom layer fluid from a tube penetrating the interface from above. Moreover, this analysis shows the comparison between withdrawal from above and withdrawal from below, especially due to the tube wall effect on the interface. Also, it attempts to explain how having large diameter compared to the capillary length would affect the analysis, which would be more representative for real SPR-like conditions.

III. EXPERIMENTAL DETAILS

A laboratory investigation was performed in order to gain insight into the conditions for which entrainment of the lighter fluid occurred for the orientations shown in Fig. 1. To record the transition from selective withdrawal to entrainment in an immiscible, two-liquid system, liquid pairs (silicon oils, brine, and water) were selected with density ratios similar to what was expected for SPR-like conditions. The liquid pairs were contained in a glass hexagonal tank approximately 25.4 cm wide and 61 cm tall. The withdrawal location was kept near the center of the container to minimize wall effects. Two withdrawal tube orientations were utilized. In the primary (SPR-like) orientation, the withdrawal tube is lowered through the interface and the lower fluid is drawn upwards (Fig. 1). In the secondary orientation, the withdrawal tube opening is placed below the interface and the lower fluid is drawn downward.

All experiments began by adjusting the withdrawal tube centered in the tank such that the inlet was perpendicular to the undisturbed interface; two Redlake MotionPro cameras positioned 120° apart were used to adjust alignment. The withdrawal tube was attached to a linear variable displacement transducer (lvdt) that was zeroed at the undisturbed interface. Prior to each experiment, the tube was lowered at least 2.54 cm below the interface of the upper fluid. The position of the tube was monitored using an lvdt (Fig. 2). The upper fluid layer was 2.54 cm thick.

In order to ensure that the return flow from the filter at the bottom of the test tank did not significantly influence the flow at the liquid-liquid interface or near the withdrawal tube, dye injection tests were conducted. The results showed that the filter distributor created a flow uniform enough to maintain the flow quality. Furthermore, tests were conducted to show that there was no change on the critical submergence depth when the location of the withdrawal tube was varied by two diameters off center or when the thickness of the oil layer was varied between 1.2 and 5.0 cm. This result is in contrast with the findings of Cohen [4] for selective entrainment above the interface, who reported that the entrainment process was affected by upper layer thickness less than 2.54 cm.

After setting the initial position of the withdrawal tube, the withdrawal rate was then slowly increased to the desired level using an impeller pump. The lower fluid was pumped into a settling tank and then back into the bottom of the tank at the withdrawal rate, maintaining a constant interface

TABLE I. Table of the properties for each fluid combination studied. ρ_u and ν_u correspond to upper fluid density and upper fluid kinematic viscosity respectively. ρ_w and ν_w correspond to lower fluid density and lower fluid kinematic viscosity respectively. γ corresponds to surface tension coefficient. The upper layer fluid consists of two variations of polydimethyl siloxane (PDMS) and for lower fluid deionized water (DI H_2O) and two variations of calcium chloride brine ($CaCl_2$ brine) were used.

	System 1	System 2	System 3	System 4	System 5	System 6
Symbols	○	∇	⋆	□	◇	△
Upper fluid	5 cSt PDMS	5 cSt PDMS	5 cSt PDMS	20 cSt PDMS	20 cSt PDMS	20 cSt PDMS
Lower fluid	DI H_2O	1.97 cSt $CaCl_2$ brine	3 cSt $CaCl_2$ brine	DI H_2O	1.97 cSt $CaCl_2$ brine	3 cSt $CaCl_2$ brine
ρ_u (g/cc)	0.918	0.918	0.918	0.950	0.950	0.950
ρ_w (g/cc)	0.998	1.245	1.325	0.998	1.245	1.325
ρ_u/ρ_w	0.920	0.737	0.693	0.952	0.763	0.717
ν_u (cSt)	5	5	5	20	20	20
ν_w (cSt)	1.01	1.97	3	1.01	1.97	3
ν_u/ν_w	4.95	2.54	1.67	19.80	10.15	6.67
γ (N/m)	0.031	0.038	0.038	0.031	0.038	0.038
l_c/d	0.44–0.94	0.22–0.46	0.20–0.41	0.57–1.21	0.23–0.49	0.20 - 0.43

depth. Keeping the flow rate constant, the tube was raised in increments of 0.25 mm until the interface neared transition, at which time the tube was raised in increments of 0.03 mm until entrainment occurred. Upon entrainment, the pump was stopped and the flow rate and tube depth were recorded. Six fluid pairs were tested in the experiments with two PDMS oils used as upper fluids and three brine solutions with varying concentrations of $CaCl_2$ as lower fluids. These combinations resulted in kinematic viscosity ratios from 1.67 to 19.80 and density ratios from 0.69 to 0.95. The surface tension for each pair was measured using a ring tensiometer and was between 0.03 and 0.038 N/m for all pairs (Table I).

For the primary orientation, three stainless steel tubes were used, with inner diameters of 0.74, 1.08, and 1.57 cm; the respective outer diameters were 0.95, 1.27, and 1.91 cm (Table II). The secondary orientation only utilized a stainless steel tube with an inner diameter of 1.08 cm. Flow rates were varied from 4.7×10^{-5} to 6.5×10^{-4} m^3/s resulting in Reynolds number (Re_d) based on the inner tube diameter ranging from 2000 to 60 000, with most cases above 10^4. Typical SPR-like situation has nominally 16 000 m^3/day of brine flowing through a 9.85-in. inner diameter tube. These flow conditions result in Re_d values on the order of 390 000 to 900 000 [1]. Assuming turbulent flow begins at Re_d values on the order of 2000 and fully turbulent at 10^4, the tube flow in the SPR caverns can be considered fully turbulent, similar to most of the experimental conditions presented.

IV. ANALYSIS

The first approach applies dimensional analysis on the normal stress balance equation. This analysis presents an idea about the forces which are important in the selective withdrawal phenomenon. The second approach uses Bernoulli's principle to explain the intuition achieved from the dimensional analysis pertaining to the experiment.

TABLE II. Withdrawal tube dimensions. All the tubes used in the experiment were stainless steel.

	Tube 1	Tube 2	Tube 3
Nominal dia. (cm)	0.953	1.27	1.905
Inner dia. (cm)	0.744	1.08	1.57

A. Interfacial stress balance

The objective of this study was to determine a predictive relationship between the submergence depth and critical flow rate at the moment of entrainment. The dimensional analysis approach on the interfacial stress balance equation allows us to scrutinize the forces acting on the interface at selective withdrawal. Surface tension manifests itself in the normal stress balance in the boundary condition for a Newtonian incompressible fluid as given below from Ref. [10], where ΔP indicates the pressure change across the interface, followed by the viscous normal stress across the interface and the surface tension stress, where γ is the surface tension and ∇ is the gradient operator:

$$\Delta P - \Delta\left(2\mu \frac{\partial u_n}{\partial \mathbf{n}}\right) - \gamma \nabla \cdot \mathbf{n} = 0. \tag{1}$$

Next, we nondimensionalize Eq. (1) with a choice to make regarding the pressure scaling. In previous works, the flow was often considered to be creeping flow [4,7,11], which resulted in a capillary number based on the capillary length as the representative nondimensional flow parameter that did not collapse our data. We therefore investigated dynamic pressure scaling and chose to bring gravity in the normal stress balance, by decomposing the pressure term into its dynamic and static component such that $P = P_d - \rho g z$, where P_d is the dynamic pressure, g is gravitational acceleration, and z is the vertical height, defined positive opposing the gravity vector, and thus $\vec{g} \cdot z$ is negative. Using $\rho_w U_0^2$ as the dynamic pressure scale, capillary length ($l_c = \sqrt{\gamma/\Delta\rho g}$) as length scale for the normal and tangential direction on the interface, tube diameter (d) as the axial or vertical length scale, and $U_0 = 4Q_{cr}/\pi d^2$ as the velocity scale, respectively, we achieve the following

equation with dimensionless variables indicated by overbars:

$$\overline{\Delta P_d} - \frac{1}{\mathrm{Fr}_d^2}\overline{\Delta\rho g z} - \frac{1}{\mathrm{Re}_{l_c}}\overline{\Delta\left(2\mu\frac{\partial u_n}{\partial \mathbf{n}}\right)} - \frac{1}{\mathrm{We}_{l_c}}\overline{\gamma\nabla\cdot\mathbf{n}} = 0, \tag{2}$$

where $\mathrm{Fr}_d = U_0/\sqrt{g'd}$ is the Froude number based on the tube diameter and g' is the reduced gravity such that $g' = (1-\rho_u/\rho_w)$, ρ_u and ρ_w are the upper fluid density and lower fluid density respectively. $\mathrm{Re}_{l_c} = \rho_w U_0 l_c/\mu_w$ is the Reynolds number based on the capillary length and $\mathrm{We}_{l_c} = \rho_w U_0^2 l_c/\gamma_s$ is the Weber number based on the capillary length.

Prior to entrainment, the location and shape of the interface is stable for a fixed flow rate, as observed from the experiment. Using order of magnitude analysis, just at the onset of entrainment, the following equation can be shown (see details in Appendix A):

$$\underbrace{\overline{\Delta P_d}}_{O(1)} - \underbrace{\frac{1}{\mathrm{Fr}_d^2}\overline{\Delta\rho g z}}_{O(10^{-1})} - \underbrace{\frac{1}{\mathrm{Re}_{l_c}}\overline{\Delta\left(2\mu\frac{\partial u_n}{\partial \mathbf{n}}\right)}}_{O(10^{-2})} - \underbrace{\frac{1}{\mathrm{We}_{l_c}}\overline{\gamma\nabla\cdot\mathbf{n}}}_{O(1)} = 0. \tag{3}$$

The scaling analysis allowed the viscous shear component to be ignored, and the dynamic pressure was found to balance surface tension with a secondary effect of buoyancy.

We defined the flow regime using the Ohnesorge number, $\mathrm{Oh}_{l_c} = \mathrm{We}_{l_c}^{\frac{1}{2}}/\mathrm{Re}_{l_c} = \mu_w/(\rho_w\gamma l_c)^{1/2}$, as illustrated in Fig. 4. Rearranging Eq. (3), we can write the following:

$$\mathrm{We}_{l_c}^{\frac{1}{2}}\overline{\Delta P_d} - \frac{\mathrm{We}_{l_c}^{\frac{1}{2}}}{\mathrm{Fr}_d^2}\overline{\Delta\rho g z} - \mathrm{Oh}_{l_c}\overline{\Delta\left(2\mu\frac{\partial u_n}{\partial \mathbf{n}}\right)} - \frac{1}{\mathrm{We}_{l_c}^{\frac{1}{2}}}\overline{\gamma\nabla\cdot\mathbf{n}} = 0. \tag{4}$$

The Ohnesorge number has previously been used in the literature to define the droplet breakout regimes of liquid jets [12]. Recently, it has also been used to analyze the regimes of selective withdrawal phenomena [13]. It enables the comparison of the viscous effect to the surface tension and inertia effect in one nondimensional parameter. In our experiment the flow regime $\mathrm{Oh}_{l_c} < 0.0085$ and also from Eq. (3), it can be inferred that the viscous effect at the onset of entertainment is negligible for our experiments. This reduces Eq. (4) into the following representative stress balance equation.

$$\overline{\Delta P_d} - \frac{1}{\mathrm{We}_{l_c}}\left[\frac{1}{(l_c/d)}\times\overline{\Delta\rho g z} + \overline{\gamma\nabla\cdot\mathbf{n}}\right] = 0. \tag{5}$$

There are three potential cases that can be considered in Eq. (5). For case 1, as $(l_c/d)\to\infty$, surface tension balances pressure and Weber number becomes dominant. For case 2, as $(l_c/d)\approx 1$, both buoyancy and surface tension act as the resistive force to balance pressure. But as the capillary length and the tube diameter are of similar order, the Weber number once again becomes the representative nondimensional parameter. For case 3, as the ratio $(l_c/d)\to 0$, buoyancy balances pressure and Froude number becomes the dominant nondimensional parameter, which is the case for actual SPR.

Thus, dimensional analysis for our case indicates that the Weber number, based on capillary length, is the representative flow parameter for the experimental data presented and is found to collapse the data well as shown in Fig. 7.

B. Inviscid flow model using Bernoulli's principle

This approach was introduced by Lubin and Springer [2] and offered a more detailed insight on the selective withdrawal phenomena. The analysis was based on the assumptions that the viscous effects are negligible and the flow is incompressible. Bernoulli's principle was applied just below the interface streamline. Lubin and Springer, in their paper, assumed a hemispherical control volume surface area, with the plug hole being at the center of the hemisphere.

In this analysis, it was already confirmed, based on the Ohnesorge number, that the viscous effect was negligible for our experimental flow field at the onset of entrainment. The assumption made by Lubin and Springer were slightly modified such that the model accounts for the suction tube instead of a drain hole on a flat tank surface. An ellipsoidal control volume surface was assumed, with the center being at an offset from the tube opening, as in Fig. 5(a). Our supposition was that the interface acts similar to a static wall and influences the isovelocity profiles away from the tube exit. An ellipsoidal control volume surface is more generalized as compared to the previously assumed spherical or hemispherical control volumes. This assumption is also supported by True and Crimaldi [14] for inhalant flows for which velocity magnitude contours near the tube opening become ellipsoidal in shape as Re increased. The ellipsoidal shape is also seen in mulitiphase Eulerian-Eulerian CFD simulations that we have performed for a few of our experimental cases; see, for example, Fig. 6.

The flow phenomena observed in this experiment is similar to the one observed by Lubin and Springer [2] and Hocking *et al.* [8,9]. At a certain entrainment depth and at a certain flow rate, a dip forms above the point sink on the surface of the lower fluid. The flow is steady unless it reaches a critical entrainment depth (S) and a critical flow rate (Q_{cr}), at which point the dip grows rapidly and extends toward the point sink almost instantaneously. Mass conservation at the ellipsoidal control volume, using the Knudsen-Thomsen approximation [15], can be expressed as

$$Q_{\mathrm{cr}} = 4\pi\alpha_0 H_d^2 U_s, \tag{6}$$

$$\alpha_0 \approx \left(\frac{b}{H_d}\right)\left[\frac{2}{3}\left\{1+\frac{1}{2}\left(\frac{b}{H_d}\right)^{\left(\frac{8}{5}\right)}\right\}\right]^{\left(\frac{5}{8}\right)}, \tag{7}$$

where Q_{cr} is the critical flow rate and H_d and b are the axes of the 2D ellipsoidal control surface. U_s is average velocity normal to the ellipsoidal surface. The deformation coefficient α_0 expresses the deviation from the spherical control surface assumption. When $\alpha_0\to 1$, the control surface is a sphere, when $\alpha_0\to 0.5$, the control surface is a hemisphere; otherwise, it is an ellipsoid. Equation (7) can be used to estimate α_0.

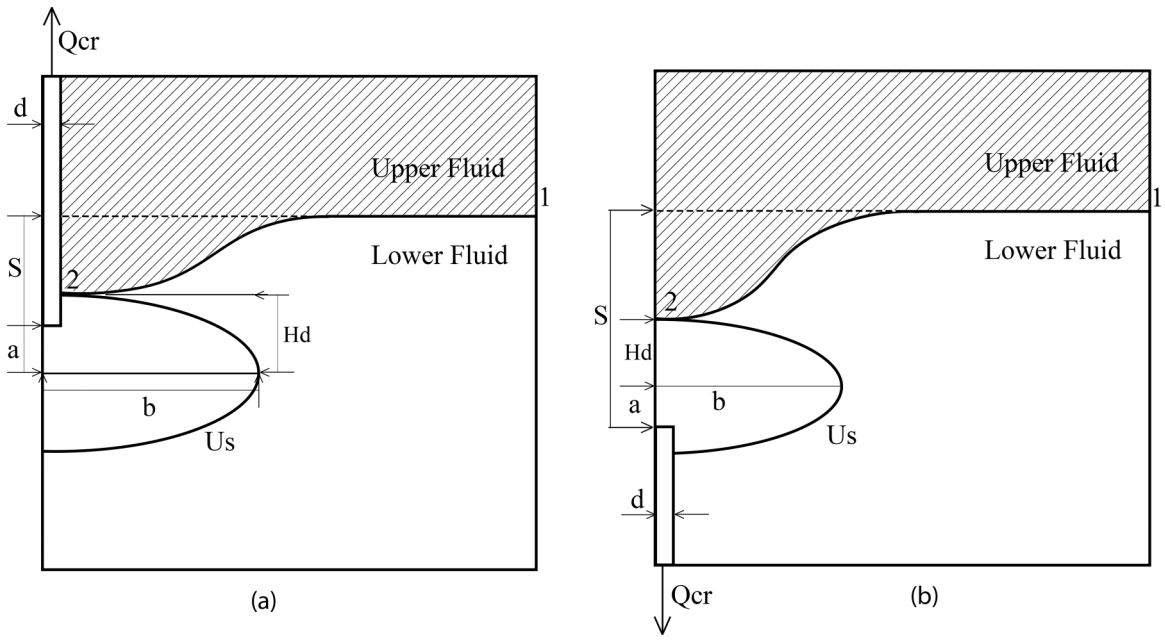

FIG. 5. Schematic of symbols and control volume used in the analysis of inviscid model. (a) Primary orientation. (b) Secondary orientation. The critical flow rate is denoted by Q_{cr}, the tube diameter by d and the submergence depth by S. H_d and b are the axes of the 2D ellipsoid. U_s is the average velocity normal to the control volume surface and a is the offset of the ellipsoidal control volume from the tube opening

Bernoulli's principle along a streamline from point 1 to point 2 in Fig. 5 generates the following equation,

$$S = H_d + \frac{U_s^2}{2g'} \mp a, \tag{8}$$

where $(-)$ is for primary orientation, $(+)$ is for secondary orientation, and a is the offset of the ellipsoidal centroid from the tube opening. Equations (6)–(8) can be rearranged to yield

$$S = H_d + \frac{Q_{\rm cr}^2}{32\pi^2 g' \alpha_0^2 H_d^4} \mp a. \tag{9}$$

The assumption of instantaneous rupture of the interface at the critical condition is used to eliminate H_d:

$$\frac{dS}{dt} \Big/ \frac{dH_d}{dt} \approx 0. \tag{10}$$

Differentiating Eq. (9) and applying Eq. (10) gives

$$H_d = \frac{0.4174}{\alpha_0^{2/5}} \left[\frac{Q_{\rm cr}^2}{g'} \right]^{\frac{1}{5}}. \tag{11}$$

Substituting H_d from Eq. (11) to Eq. (9) yields

$$S = \frac{0.5227}{\alpha_0^{2/5}} \left[\frac{Q_{\rm cr}^2}{g'} \right]^{\frac{1}{5}} \mp a. \tag{12}$$

Normalizing Eqs. (11) and (12) with the diameter allows us to rewrite the equations in terms of Weber number $\mathrm{We}_{l_c} = \rho_w Q_{cr}^2 l_c / d^4 \gamma$ and capillary length $l_c = \sqrt{\gamma/\Delta\rho g}$, such that it provides a linear relationship between the nondimensionalized critical entrainment depth and nondimensionalized critical flow rate raised to the power 1/5:

$$\frac{S}{d} = \frac{0.5227}{\alpha_0^{2/5}} \left(\frac{l_c}{d} \right)^{\frac{1}{5}} \mathrm{We}_{l_c}^{\frac{1}{5}} \mp \frac{a}{d}, \tag{13}$$

$$\frac{H_d}{d} = \frac{0.4174}{\alpha_0^{2/5}} \left(\frac{l_c}{d} \right)^{\frac{1}{5}} \mathrm{We}_{l_c}^{\frac{1}{5}}. \tag{14}$$

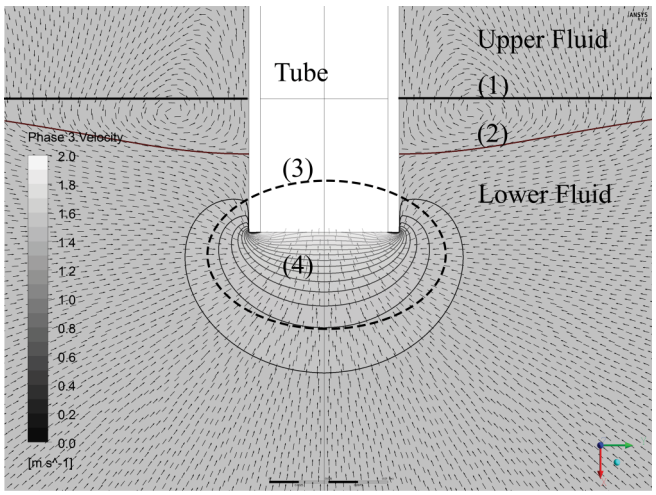

FIG. 6. An example multiphase Eulerian-Eulerian CFD simulation for system 4, withdrawal of bottom layer fluid at subcritical flow rate using Ansys FLUENT [16]. Label (1) denotes the initial position of the undisturbed interface; label (2) denotes an equilibrium position of the interface; label (3) denotes the control volume where the velocity vectors are perpendicular to the ellipsoidal control surface (dashed line); and label (4) denotes isovelocity contours.

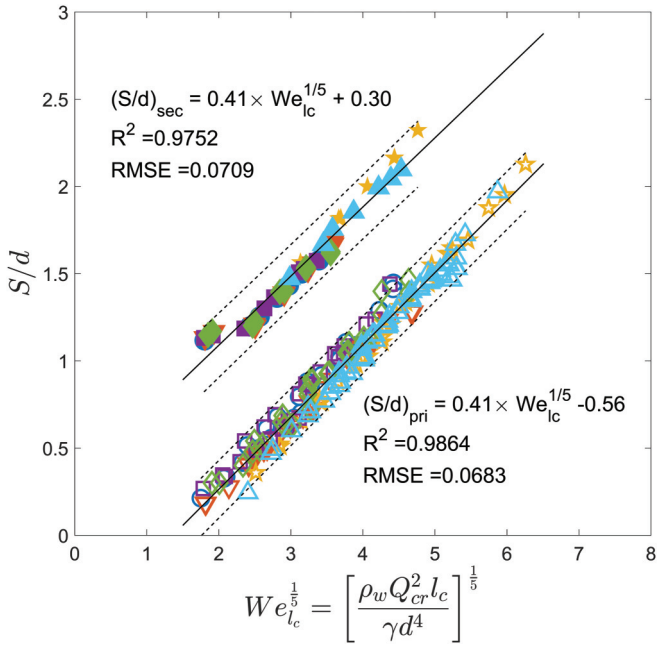

FIG. 7. Critical submergence depth as a function of critical Weber number. The "hollow" symbols represent the primary orientation data, whereas the "filled" ones represent the secondary orientation data. The solid line through the hollow symbols is the best linear fit for the primary orientation and the solid line through the filled symbols is the best linear fit for the secondary orientation. The dotted lines are 95% prediction intervals. The region above the 95% upper bound of entrainment depth is selective withdrawal zone, whereas the area below is entrainment zone. The symbols are defined in Table I.

V. RESULTS AND DISCUSSION

We now apply Eq. (13) to our experimental data for both orientations and present the results in Fig. 7. The relation for entrainment depth as a function of Weber number to the one-fifth power fits the data well. Additionally, expressions for α_0, a, and b can easily be estimated from the slope and intercept values of the fitted equation as shown in Table IV.

From this analysis, it can also be concluded that the experiment by Lubin and Springer is a special case of the proposed model, where $\alpha_0 = 0.5$ (for hemispherical control volume surface) and the fluid layers were chosen such that $(l_c/d)^{1/5} \approx 1$; see Table III. The point sink was assumed to be exactly on the plug-hole opening, rendering $a = 0$. Using these assumptions in Eqs. (6), (11), and (12), as well as taking help from Eq. (B4), the expression derived by Lubin in Eq. (15) is realized:

$$\frac{S}{d} = 0.69\left[\frac{Q_{\rm cr}^2}{g' d^5}\right]^{\frac{1}{5}}. \tag{15}$$

TABLE III. Fluid properties for calculating ratio of capillary length to tube diameter for Lubin's paper [2].

ρ_1 (kg/m^3)	ρ_2 (kg/m^3)	γ (N/m)	d (m)	l_c (m)	$(l_c/d)^{(1/5)}$
998	1.2226	0.075	0.0032	0.003	0.99
998	783.43	0.04	0.0032	0.004	1.05
998	918.16	0.021	0.0064	0.005	0.95
998	918.16	0.038	0.0064	0.007	1.02
998	868.26	0.012	0.0032	0.003	0.99

For an individual critical Weber number, the fit equations lead to a critical nondimensional submergence depth for the corresponding tube orientations, Fig. 7. For cases when the viscous effect is negligible compared to the surface tension and inertial effect (low Oh_{l_c} flow), and the capillary length is in the comparable order of scale to the tube diameter, a predictive relationship is generated for the desired selective withdrawal, above the curve, and entrainment, below the curve.

The offset between the primary and the secondary orientation can be explained as the effect of the tube wall on the interface. In the primary orientation, the tube wall is in contact with the interface and impedes the entrainment whereas in the secondary orientation the interface is completely free from any surface contact. As a result, for the same submergence depth the primary orientation requires a stronger flow rate compared to the secondary orientation for entrainment to occur. A point to be noted here is that having a negative entrainment depth would require the lower fluid to "stick" to the withdrawal tube and block the upper fluid from being entrained.

It is evident from the analysis that the ratio (l_c/d) plays a significant role in shaping the ellipsoid; see Table IV for parameters. The inverse Bond number can be defined as (l_c/d), with details in Appendix B. It can be interpreted that Bo^{-1} is the scaled surface tension effect with respect to the buoyancy effect at the diameter scale. From the normal stress balance, Eq. (5), buoyancy dominates surface tension for large diameters and the Bo^{-1} reduces to a small number. In SPR-like cavern flows, the tube diameter is large compared to the capillary length, so it can be inferred that the force balance is one of buoyancy balancing pressure and, consequently, the Froude number is expected to be the representative nondimensional number, and the correlation shown in Fig. 7 is not claimed to be predictive. However, for the experiments presented herein, the inverse Bo numbers range from about 0.2 to 1.2, which is in the vicinity of case 2 and makes the Weber number the representative nondimensional number at entrainment.

In this experiment, during selective withdrawal, the reduction of pressure due to the tube velocity creates a downward pull on the interface toward the tube inlet. The surface tension and the buoyancy create a resistance to this force and at equilibrium, a steady state, subcritical balance is achieved such as shown in the left photo in Fig 1. When $\mathrm{Bo}^{-1} > 1$, surface tension dominates as the resistive force and when $\mathrm{Bo}^{-1} < 1$, buoyancy dominates. Entrainment occurs when the resistive force is overcome by the force due to the pressure reduction.

To understand the effect on inverse Bond number on the shape of the ellipsoidal control volume, a simulation was conducted keeping the flow rate fixed for a chosen fluid combination. A high flow rate of 0.35 m^3/s was chosen so that the high Reynolds number flow condition was satisfied even for the largest diameter and viscous effect can be neglected ($\mathrm{Re}_{l_c} \approx 10^3$ to 10^8). It corresponds to very low Ohnesorge number ($\mathrm{Oh}_{l_c} \approx 10^{-4}$ to 10^{-2}) for the simulation. The inverse

TABLE IV. Table of estimations for the parameters α_0, a, and b, with uncertainties of the slope and the intercept given parenthetically.

Orientation	Slope	Intercept	α_0	a (m)	b (m)
Primary	$0.41(\pm\ 0.01)$	$-0.56(\pm\ 0.04)$	$1.84(l_c/d)^{\frac{1}{2}}$	$0.56d$	$H_d[-1+\{1+7.92(l_c/d)^{\frac{4}{5}}\}^{\frac{1}{2}}]^{\frac{5}{8}}$
Secondary	$0.41(\pm\ 0.03)$	$+0.30(\pm\ 0.08)$	$1.95(l_c/d)^{\frac{1}{2}}$	$0.30d$	$H_d[-1+\{1+8.75(l_c/d)^{\frac{4}{5}}\}^{\frac{1}{2}}]^{\frac{5}{8}}$

Bond number, $\mathrm{Bo}^{-1} = (l_c/d)$ was varied by changing the surface tension coefficient and the diameter. The range of the surface tension coefficient was from 0.001 to 0.1 N/m. Eight selected diameters were chosen from a very wide range of 0.001 to 0.30 m.

The inverse Bond number, according to the derived model, shapes the major and minor axes of the ellipsoidal control volume surface. Figure 8(a) shows the trend of H_d, b for the primary orientation as a function of Bo^{-1}. The trend for the secondary orientation Fig. 8(b) was found to be similar to the primary. For both orientations, the ellipsoid becomes a sphere at a particular Bo^{-1} value. As the Bo^{-1} increases, H_d tends to decrease, indicating the lowering of interface, Fig. 5. The interface acts like a static wall and consequently, as the interface drops, it also reduces the velocity in its vicinity. At some critical average velocity U_s, the interface cannot resist the downward pull anymore and it collapses. To collapse at a reduced critical velocity the area of the control surface has to increase, as the Bo^{-1} increases. The only way the control surface area can increase for a fixed flow rate is by an increase of the parameter b, which is evident in Fig. 8. Figure 8(c) shows the results of extending the analysis to fluids in Lubin's experimental setup. It is apparent that as Bo^{-1} gets closer to 1, the major and minor axes becomes equal and the control volume shape obtains the form of an hemisphere, as Lubin and Spring assumed in his paper.

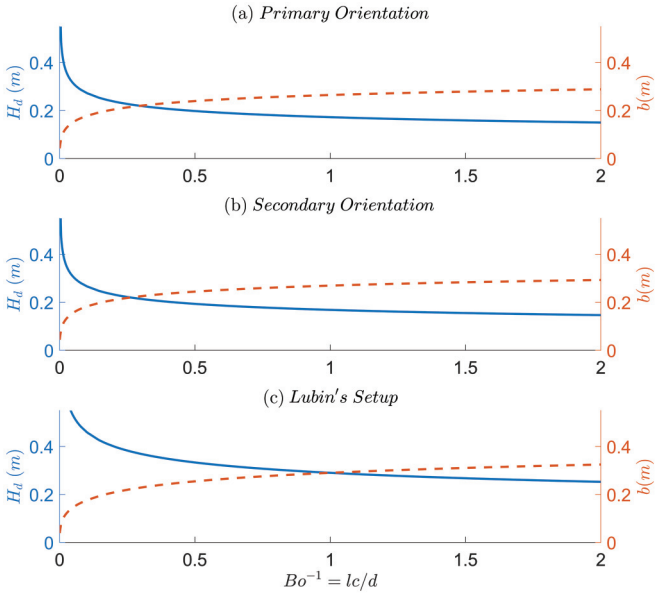

FIG. 8. Ellipsoidal control volume parameters (H_d, b) as a function of the inverse Bond number for (a) primary orientation, (b) secondary orientation, and (c) Lubin and Springer model. The fluid combination of system 3 (Table I) was chosen. The flow rate was set to be 0.35 m^3/s. The surface tension coefficient was varied from 0.001 to 0.1 N/m and eight selected diameters were chosen from a very wide range of 0.001 to 0.30 m. The solid line is for plotting H_d and the dashed line is for plotting b.

VI. CONCLUSION

This paper presented two approaches to predict transition from selective withdrawal to entrainment using the physics of fluid flow. The first used the dimensional analysis approach on the normal stress balance equation showed the Weber number as the relevant nondimensional parameter specific to selective withdrawal. Moreover, this method provided a representation for the force balance on the interface for the relative significance of buoyancy, surface tension, and pressure balance. The second used Bernoulli's principle for selective withdrawal with two withdrawal-tube orientations. The theoretical model was fitted using experimental data and the expressions for corresponding unknown parameters were derived. It is shown that the general control volume associated with the average velocity at the critical flow rate is ellipsoidal in shape. It was also shown that Lubin's correlation is a special case of this proposed model. Both approaches led to predictive relations for the selective entrainment depth as a function of the critical Weber number raised to the one-fifth power.

ACKNOWLEDGMENTS

The experimental work was performed at Sandia National Laboratories with Joel Hartenberger, Tim O'Hern, and Stephen Webb.

APPENDIX A: ORDER OF MAGNITUDE ANALYSIS

Order of magnitude analysis for each term of Eq. (3) can be performed using the appropriate scales.

We analyze $\overline{\Delta P_d}$ term,

$$\overline{\Delta P_d} = \frac{\left(\rho_w U_i^2 - \rho_u U_i^2\right)}{\rho_w U_0^2} \approx O\left(\frac{U_i^2}{U_0^2}\right), \tag{A1}$$

where $U_i(\approx Q_{\mathrm{cr}}/4\pi l_c^2)$ is the velocity estimated close to the interface. The maximum order of the ratio U_i/U_0 becomes 10^{-1}:

$$\overline{\Delta P_d} = \frac{\left(\rho_w U_i^2 - \rho_u U_i^2\right)}{\rho_w U_0^2} \approx O(10^{-2}). \tag{A2}$$

We analyze the $\frac{1}{\mathrm{Fr}_d^2}\overline{\Delta\rho g z}$ term,

$$\overline{\Delta\rho g z} = \frac{(\rho_w g z_w - \rho_u g z_u)}{\rho_w g' d} \approx O\left(\frac{\rho_w g z_w}{\rho_w g' d}\right). \tag{A3}$$

The maximum depth that z can have is in the order of the submergence depth S, so the maximum order becomes

$$\overline{\Delta\rho g z} = \frac{(\rho_w g z_w - \rho_u g z_u)}{\rho_w g' d} \approx O(1). \tag{A4}$$

Similarly, for the Froude number we can find the maximum order to be

$$\frac{1}{\mathrm{Fr}_d^2} = \frac{g' d}{U_0^2} \approx \frac{10 \times 10^{-2}}{10^2} \approx O(10^{-3}). \tag{A5}$$

The order of the total product becomes

$$\frac{1}{\mathrm{Fr}_d^2}\overline{\Delta\rho g z} \approx O(10^{-3}). \tag{A6}$$

We analyze the $\frac{1}{\mathrm{Re}_{l_c}}\overline{\Delta(2\mu\frac{\partial u_n}{\partial n})}$ term,

$$\overline{\Delta\left(\mu\frac{\partial u_n}{\partial n}\right)} = \frac{\mu_w \frac{\Delta u_n^w}{\Delta n} - \mu_w \frac{\Delta u_n^u}{\Delta n}}{\mu_w \frac{U_0}{l_c}}. \tag{A7}$$

Below the interface, for the withdrawal fluid, it can be estimated that the velocity goes from almost zero (compared to tube velocity) near the interface to U_0 near the tube, over the length scale l_c. Above the interface, for the upper fluid, it can be estimated that the velocity goes from almost zero near the interface to some maximum normal velocity $U_n^m (\approx 4Q_{\mathrm{cr}}/\pi l_c^2)$ over the length scale l_c. Using these estimated scales, we can rewrite Eq. (A7) as below:

$$\overline{\Delta\left(\mu\frac{\partial u_n}{\partial n}\right)} \approx O\left(\frac{\mu_u U_n^m}{\mu_w U_0}\right) \approx O(10). \tag{A8}$$

Similarly, for the Reynolds number we can find the order to be

$$\frac{1}{\mathrm{Re}_{l_c}} = \frac{\mu_w}{\rho_w U_0 l_c} \approx \frac{10^{-3}}{10^3 \times 10 \times 10^{-2}} \approx O(10^{-5}). \tag{A9}$$

The order of the product becomes

$$\frac{1}{\mathrm{Re}_{l_c}}\overline{\Delta\left(2\mu\frac{\partial u_n}{\partial n}\right)} \approx O(10^{-4}). \tag{A10}$$

We analyze the $\frac{1}{\mathrm{We}_{l_c}}\overline{\gamma\nabla\cdot\mathbf{n}}$ term,

$$\overline{\gamma\nabla\cdot\mathbf{n}} = \frac{\gamma\nabla\cdot\mathbf{n}}{\gamma_s l_c} \approx O\left(\frac{\nabla\cdot\mathbf{n}}{l_c}\right), \tag{A11}$$

where $\nabla\cdot\mathbf{n}$ is the curvature and from our experiment it is in the order of 10:

$$\overline{\gamma\nabla\cdot\mathbf{n}} \approx O\left(\frac{\nabla\cdot\mathbf{n}}{l_c}\right) \approx O(10^3). \tag{A12}$$

The order of Weber number in our experiments are

$$\frac{1}{\mathrm{We}_{l_c}} = \frac{\gamma_s}{\rho_w U_0^2 l_c} \approx \frac{10^{-2}}{10^3.10^2.10^{-2}} \approx O(10^{-5}). \tag{A13}$$

The order of the product is as following,

$$\frac{1}{\mathrm{We}_{l_c}}\overline{\gamma\nabla\cdot\mathbf{n}} = \approx O(10^{-2}). \tag{A14}$$

APPENDIX B: BOND NUMBER

The Froude number for two-fluid stratified flow is defined as the ratio of flow inertia to buoyancy effect [17,18], $\mathrm{Fr}_{L_1} = U_0/\sqrt{g' L_1}$, where g' is the reduced gravity such that $g' = (1 - \rho_u/\rho_w)$, assuming $\rho_w > \rho_u$. Similarly, the ratio of inertia to surface tension effect is defined as Weber number [17], $\mathrm{We}_{L_2} = (\rho_w U_0^2)/(\gamma_s/L_2)$. When comparing Froude number to the Weber number, another dimensionless number, known as the Bond number [17], comes into effect. The Bond number is defined as the ratio of buoyancy effect to surface tension effect, $\mathrm{Bo} = (\rho_w g' L_1)/(\gamma_s/L_2)$. The squared Froude number can be rewritten as

$$\mathrm{Fr}_{L_1}^2 = \frac{U_0^2}{g' L_1} = \frac{\rho_w U_0^2 L_2}{\gamma_s} \times \frac{\gamma_s}{\rho_w g' L_1 L_2}, \tag{B1}$$

$$\mathrm{Fr}_{L_1}^2 = \mathrm{We}_{L_2}/\mathrm{Bo}. \tag{B2}$$

The dimensional analysis approach uses length scales $L_1 = L_2 = l_c$. Using the definition of capillary length, l_c, the Bond number reduces to $\mathrm{Bo} = 1$. Applying this in Eq. (B2) yields

$$\mathrm{Fr}_{l_c}^2 = \mathrm{We}_{l_c}. \tag{B3}$$

Similarly, if the length scales were such that $L_1 = d$ and $L_2 = l_c$, the Bond number reduces to $\mathrm{Bo} = d/l_c$. Applying this in Eq. (B2) yields

$$\mathrm{Fr}_d^2 = \mathrm{We}_{l_c}/\mathrm{Bo} = \left(\frac{l_c}{d}\right)\mathrm{We}_{l_c}. \tag{B4}$$

Equations (B3) and (B4) helps us express the Froude numbers in terms of Weber numbers.

[1] J. D. Hartenberger and T. J. O'Hern, *Proceeding of the ASME 2011 International Mechanical Engineering Congress and Exposition*, Paper No. IMECE2011-66278 (ASME, Colorado, USA, 2011), pp. 1299–1307.

[2] B. T. Lubin and G. Springer, J. Fluid Mech. **29**, 385 (1967).

[3] I. Cohen and S. R. Nagel, Phys. Rev. Lett. **88**, 074501 (2002).

[4] I. Cohen, Phys. Rev. E **70**, 026302 (2004).

[5] S. C. Case and S. R. Nagel, Phys. Rev. Lett. **98**, 114501 (2007).

[6] F. Blanchette and W. W. Zhang, Phys. Rev. Lett. **102**, 144501 (2009).

[7] J. R. Lister, J. Fluid Mech. **198**, 231 (1989).

[8] D. E. Farrow and G. C. Hocking, J. Fluid Mech. **549**, 141 (2006).

[9] G. C. Hocking, H. H. N. Nguyen, L. K. Forbes, and T. E. Stokes, ANZIAM J. **57**, 417 (2016).

[10] W. M. Deen, *Analysis of Transport Phenomena*, Topics in Chemical Engineering (Oxford University Press, Oxford, UK, 2011)

[11] M. K. Berkenbusch, I. Cohen, and W. W. Zhang, J. Fluid Mech. **613**, 171 (2008).

[12] J. Eggers and E. Villermaux, Rep. Prog. Phys. **71**, 036601 (2008).
[13] Z. Pan, J. K. Nunes, and H. A. Stone, Phys. Rev. Lett. **125**, 264502 (2020).
[14] A. C. True and J. P. Crimaldi, Phys. Rev. E **95**, 053107 (2017).
[15] M. S. Klamkin, Am. Math. Monthly **78**, 280 (1971).
[16] ANSYS, FLUENT, product release 19.1,2018.
[17] F. M. White, *Fluid Mechanics*, 8th ed. (McGraw-Hill Education, New York, 2016).
[18] F. Tang, L. Li, M. Dong, Q. Wang, F. Mei, and L. Hu, Appl. Therm. Eng. **110**, 1021 (2017).

Correction: A production error resulted in disappearance of a data symbol in the second sentence of the caption to Figure 4 and has been remedied.